



Cite this: *Nanoscale*, 2016, **8**, 15505

Received 29th April 2016,
Accepted 3rd August 2016

DOI: 10.1039/c6nr03488h

www.rsc.org/nanoscale

Slanted gold mushroom array: a switchable bi/tridirectional surface plasmon polariton splitter†

Yang Shen,‡^{a,c} Guisheng Fang,‡^a Alexander Cerjan,‡^b Zhenguo Chi,^c Shanhui Fan*^b and Chongjun Jin*^a

Surface plasmon polaritons (SPPs) show great promise in providing an ultracompact platform for integrated photonic circuits. However, challenges remain in easily and efficiently coupling light into and subsequently routing SPPs. Here, we theoretically propose and experimentally demonstrate a switchable bi/tridirectional beam splitter which can simultaneously perform both tasks. The photonic device consists of a periodic array of slanted gold ‘mushrooms’ composed of angled dielectric pillars with gold caps extruding from a periodic array of perforations in a gold film. The unidirectional coupling results from the interference of the in-plane guided modes scattered by a pair of dislocated gold gratings, while the output channel is determined by the polarization of the incident beam. This device, in combination with dynamic polarization modulation techniques, has the potential to serve as a router or switch in plasmonic integrated circuits.

One of the primary objectives of research in modern information processing is to achieve the fastest rates of computation and data transmission with a minimal footprint on an integrated circuit.¹ Unfortunately, conventional semiconductor electronics have nearly reached their fundamental limits due to heat generation and interconnect delay-time issues,² which has in turn spurred interest in harnessing the intrinsic speed of photons for on-chip applications.³ Despite possessing an incredible data transmission rate, dielectric photonics are restricted by the diffraction limit of light, requiring wavelength-scale features to prevent spreading, and resulting in prohibitively large device sizes.⁴ As a result, surface plasmon polaritons (SPPs) have emerged as a potential solution for a

next-generation integrated circuit that combines the ultracompact critical feature sizes of nanoelectronics with the extremely high transmission speeds of dielectric photonics, due to their ability to squeeze light into the nanoscale region near the metal/dielectric interface.⁵

A critical challenge in designing a plasmonic integrated circuit is ensuring efficient generation of SPPs while retaining tunable control over their propagation direction. Recently, there have been substantial efforts in achieving unidirectional SPP excitation by breaking the system’s symmetry, either by changing the properties of the incident light or altering the geometry of the coupling element. For example, using specially designed metasurfaces and slots, unidirectional SPPs have been dynamically launched by varying the incident angle of a linearly polarized beam or the helicity of a circularly polarized beam.^{6–11} However, these methods either require mechanical adjustments to change the beam’s incident angle, or the additional external optical elements necessary to produce circularly polarized incident light. Asymmetrical gratings,¹¹ slits,^{12–15} grooves,^{16,17} and cavities^{18,19} have been demonstrated as efficient unidirectional SPP couplers using normal light illumination, but the direction of SPP excitation in these couplers is predefined during fabrication, and cannot be dynamically reconfigured.

In addition to the challenges associated with coupling to the SPP, a second difficulty arises in achieving controllable routing for the optical signals in an integrated circuit. Basic SPP beam splitters and demultiplexers have been demonstrated using nanoparticle chains,^{20–23} nanowires,^{24–26} nanogaps^{27,28} and nanogratings,^{29–31} but active control of the splitting is still absent in these types of devices without changing the underlying structure. Recently, branched nanowires were demonstrated as an SPP router,^{32,33} for which the SPP can be switched between the main and branch wires by controlling the polarization of the incident light. Routing, splitting, and directional coupling have also been recently demonstrated using slot-waveguide-based optical nanocircuits integrated with an electrically driven nanoscale on-chip light-emitting diode (LED).³⁴

^aState Key Laboratory of Optoelectronic Materials and Technologies, School of Materials Science and Engineering, Sun Yat-sen University, Guangzhou 510275, China. E-mail: jinchjun@mail.sysu.edu.cn

^bDepartment of Electrical Engineering, Ginzton Laboratory, Stanford University, Stanford, CA 94305-4088, USA. E-mail: shanhui@stanford.edu

^cSchool of Chemistry and Chemical Engineering, Sun Yat-sen University, Guangzhou 510275, China

†Electronic supplementary information (ESI) available. See DOI: 10.1039/c6nr03488h

‡These authors contributed equally to this work.

Here we propose and realize a single photonic element that is capable of both SPP directional coupling and splitting simultaneously based on a two-dimensional periodic array of slanted gold ‘mushrooms’, which is composed of angled dielectric pillars with gold caps extruding from a periodic array of holes in a gold film. In our proposed device, unidirectional coupling results from the interference of the in-plane guided modes scattered by a pair of dislocated gold gratings, while the output channel is determined by the polarization of the incident beam. Thus, this device, in combination with dynamic polarization modulation techniques, has the potential to serve as a router or a switch in plasmonic integrated circuits.

Most schemes for generating unidirectional SPPs rely upon creating multiple scattered waves generated by metallic nanoparticles,²¹ slits,^{6,35–38} or apertures,^{7,8} which constructively interfere in the desired direction, while destructively interfering in the opposite direction.³⁹ However, pure metallic nanoparticle chains have a high dissipative loss, limiting their overall coupling efficiency.²⁷ Furthermore, both slot- and aperture-based devices rely upon coupling the transmission through narrow apertures to SPPs, such that the overall coupling efficiency is very difficult to quantify.^{7–9} Recently, an efficient SPP unidirectional coupler based on a one-dimensional dislocated double-layered metal grating was demonstrated.⁴⁰ Here, we extend this principle to a two-dimensional in-plane system to accomplish SPP directional coupling and routing simultaneously. The core of our device is a slanted gold mushroom array (SGMA) covering an area of $3 \times 3 \mu\text{m}^2$ (Fig. 1a), which is composed of a square lattice of gold-capped inclined photoresist pillars, periodically positioned in a perforated gold film on top of a substrate. In a single unit cell of the SGMA, the upper square gold cap with a side length w_1 and thickness t has a non-zero in-plane dislocation Δs with respect to the lower square hole (Fig. 1b and c), where $\Delta s = \sqrt{(\Delta x)^2 + (\Delta y)^2}$, and Δx and Δy refer to the dislocations in x - and y -axes, respectively. The tilting angle, side length and height of the slanted pillars are denoted by α , w_2 and h , respectively, and the lattice constant of the array is given by a . Here, we define the orientations of the in-plane dislocations as (1,0), (0,1) and (1,1), which correspond to the directions of the displacements projected onto the xy -plane. Similar definitions are adopted to describe the polarizations of the incident light.

There are two conditions for generating directional SPPs in a dislocated structure. First, due to the translational invariance of the structure, the vacuum wavelength of the normal incident light, λ_0 , must be matched to the periodicity of the structure⁴⁰ (the detailed derivation can be found in the ESI†).

$$\left(\frac{2n_{\text{eff}}}{\lambda_0}\right)^2 - \left(\frac{m_z}{h'}\right)^2 = \left(\frac{2m_x}{a}\right)^2 + \left(\frac{2m_y}{a}\right)^2 \quad (1)$$

in which $h' = h - t$ is the distance between the upper and lower gold arrays and n_{eff} is the effective refractive index between the two arrays. Here, m_x and m_y are integers, which are related to

the wave vector of the guided mode in the x and y directions respectively, and m_z is the non-negative integral number of half-wavelengths residing between the upper and lower gold arrays. As such, the longest incident wavelength resulting in propagating modes can actually yield four degenerate SPPs, which either travel along the $\pm x$ - or $\pm y$ -axis. Second, unidirectional SPPs must be excited along the orientation of the polarization (electric field) of the normal incident waves. Thus, to launch a unidirectional SPP in a particular direction, the incident light must be chosen to both satisfy eqn (1) and have a polarization component along the propagation axis. That is to say, for a predefined SGMA, one can control the branched coupling of SPPs that are split into the two orthogonal channels by tailoring the polarization orientation of the incident electric field, with the wavelength matched to the lowest order propagating modes of eqn (1).

To gain further insight into the optical properties of the SGMA-based bi/tridirectional splitter, we performed numerical simulations using the finite-difference time-domain (FDTD) method (FDTD Solutions, Lumerical). Fig. 1d compares the simulated absorption spectra of (1,0)-polarized light normally incident upon an infinite SGMA(1,1) (black curve), with $\Delta x = 55 \text{ nm}$ and $\Delta y = 55 \text{ nm}$, and an infinite normal gold mushroom array (NGMA, red curve), for which the upper metal array is not displaced relative to the lower array, $\Delta x = 0 \text{ nm}$ and $\Delta y = 0 \text{ nm}$. The other parameters of the system were held constant for both simulations, $a = 640 \text{ nm}$, $h = 550 \text{ nm}$, $w_1 = 255 \text{ nm}$, $w_2 = 225 \text{ nm}$, and $t = 100 \text{ nm}$. These parameters correspond to a nearly maximal extinction ratio for the SGMAs (the effects of the lattice constant, dislocation between the top and bottom gold array and waist diameter of the incident Gaussian beam on the unidirectional coupling efficiency and extinction ratio can be seen in ESI Fig. S1†). As can be seen, an additional narrow peak ($\lambda = 796 \text{ nm}$) within a broad dip appears for the SGMA, but is absent for the NGMA (Fig. 1d). The distribution of the electric field component E_z at the x - z plane reveals that this wavelength corresponds to a guided mode featuring a strongly localized electric field inside the air/dielectric layer between the upper and lower gold arrays (Fig. 1e). The power flow density along the x -axis, P_x , shows a $+x$ -direction power flowing, confirming the unidirectional effect of this mode (Fig. 1f). To further demonstrate the SGMA as a realistic bi/tridirectional splitter, we performed simulations for the devices with a 5×5 SGMA embedded in a uniform gold film. A collimated Gaussian beam with a waist diameter D of 3000 nm was applied to normally impinge the device at the optimal wavelengths where the largest extinction ratio is achieved (see ESI Fig. S2†). In Fig. 1g and h, we show the electric field intensity distributions in the x - y plane (4 nm above the top surface of the bottom gold film) of an SGMA(1,1) under (1,1)- and (1,0)-polarized illumination, respectively. For the incident light with (1,1)-polarization (Fig. 1g), two propagating SPP waves along the $+x$ - and $+y$ -directions are observed moving away from the center of the SGMA(1,1) (‘bidirectional splitter’ state). While for the same device under (1,0)-polarized illumination (Fig. 1h), three propagating SPP waves are present, travelling

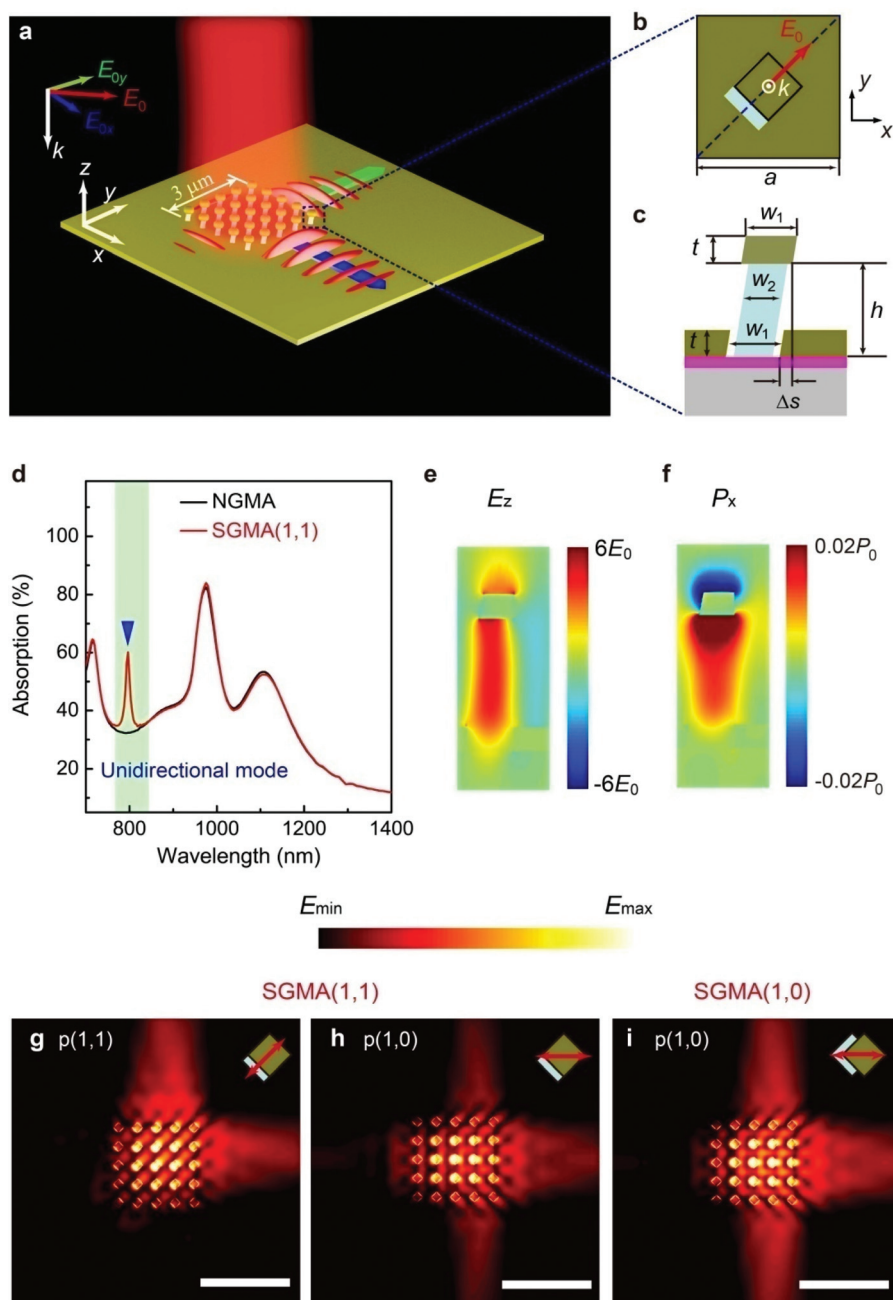


Fig. 1 Two-dimensional arrays of the slanted subwavelength gold mushroom as polarization-mediated SPP beam splitters. (a) Schematic showing the configuration of a polarization-selective SPP beam splitter based on an SGMA(1,1). An in-plane linear polarization E_0 (red) can be decomposed into the two orthogonal components E_{0x} (blue) and E_{0y} (green), leading to the polarization-dependent unidirectional couplings along x - and y -axes, respectively. (b) Schematic of single unit cell from the top view. (c) Schematic of single unit cell from the cross-sectional view (through the blue dashed line in (b)). Throughout the paper, the geometrical parameters of the SGMA are fixed as follows: lattice constant $a = 640$ nm, pillar height $h = 550$ nm, the thickness of the deposited gold layer $t = 100$ nm, the side lengths of the gold cap and hole $w_1 = 255$ nm and the pillar $w_2 = 225$ nm, respectively. (d) Simulated absorption spectra of the infinite NGMA ($\Delta x = 0$ nm, $\Delta y = 0$ nm, black curve) and SGMA(1,1) ($\Delta x = 55$ nm, $\Delta y = 55$ nm, red curve) under normal incident waves with (1,0)-polarization. (e, f) Simulated distributions of electric field intensity component E_z and power flow density component P_x at the x - z plane formed by cutting along the diagonal of the bottom square hole for the above SGMA in (d), respectively. (g, h) Simulated electric field intensity distributions at x - y plane (4 nm above the top surface of the bottom gold film) for a 5×5 SGMA(1,1) under the incident illumination with (1,1)- and (1,0)-polarizations. (i) Simulated electric field intensity distributions at x - y plane for a 5×5 SGMA(1,0) under the incident illumination with (1,0)-polarization. The excitation wavelengths in the above three cases are all 780 nm. (g–i) Scale bars, 3000 nm.

along the $+x$ - and $\pm y$ -directions ('tridirectional splitter' state), which is similar to the case of the SGMA(1,0) when subjected to (1,0)-polarized light (Fig. 1i). It is noted that, due to the presence of constructive interference, the SPP power flow along the $+x$ direction is higher than two symmetrical SPP power flows along $\pm y$ -directions. In fact, both the bidirectional splitter state (Fig. 1g) and the tridirectional splitter states (Fig. 1h and i) demonstrate a consistent coupling to a unidirectional guided plasmon mode, depending upon the polarization of the incident light with respect to the direction of in-plane dislocations of the SGMA. This suggests that our SGMA holds the promise of switchable bi/tridirectional splitting.

We employed two-beam interference lithography twice combined with shadow evaporation of gold to fabricate SGMAs (Fig. 2a). To create an in-plane dislocation Δs between the upper gold caps and lower gold holes, we first patterned a periodic array of slanted photoresist pillars in a square lattice using two iterations of tilted two-beam interference lithography, where the sample was tilted at the angles α_1 and α_2 about the x - and y -axes (Fig. 2b). To finish the SGMA, an

oblique gold deposition was then performed in the direction parallel to the photoresist pillars. By adjusting the rotation angles (α_1, α_2) of the samples in each exposure, one can readily prepare the slanted mushroom arrays with varying dislocation orientations, i.e. SGMA(1,0) or SGMA(1,1). The fabrication procedure can be found in the ESI.† Fig. 2c–e and f–h show the top-view and cross-sectional scanning electron microscopy (SEM) images of NGMA, SGMA(1,0) and SGMA(1,1), respectively. For these mushroom arrays, the lattice constants (a_x, a_y) are determined by the incident angles of the laser beams (φ_1, φ_2) and the rotation angles (α_1, α_2). The spacing between the top and bottom gold layer is determined by the thickness h of the photoresist layer.

To examine the unidirectional mode observed in the fabricated SGMAs, we recorded the reflectance spectra of the NGMA and SGMAs at normal incidence with varying polarized orientations (solid curves in Fig. 3) via an ultraviolet/visible/near-infrared spectrometer (Lambda 950, PerkinElmer). A normal illumination element, consisting of one beam splitter and three silver mirrors was placed in the optical path, as

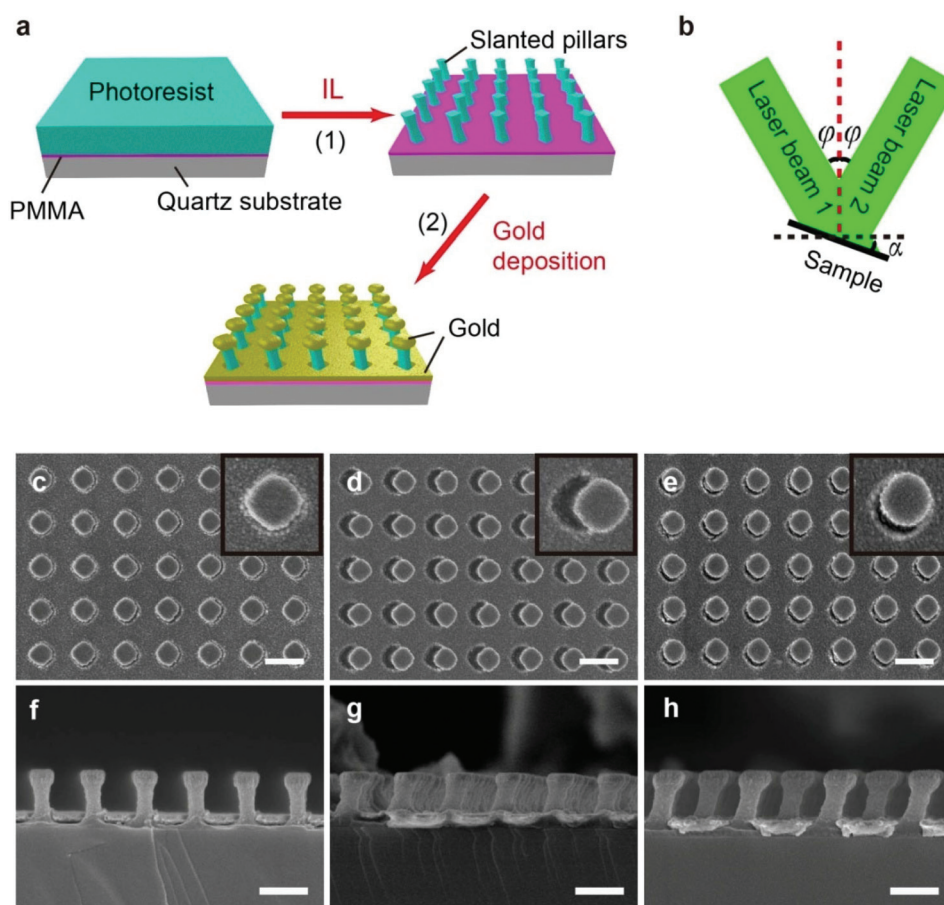


Fig. 2 SGMA fabrication. (a) Schematic showing the fabrication procedure of SGMAs. IL stands for interference lithography, and PMMA refers to poly(methyl methacrylate). (b) Tilted interference lithography set-up for preparing the slanted photoresist pillar arrays. φ is the incident angle of the two laser beams with respect to the normal (red dashed line), and α is the tilting angle of the sample. (c–e) Top-view SEM images of NGMA, SGMA(1,0) ($\Delta x = 100$ nm) and SGMA(1,1) ($\Delta x = 55$ nm, $\Delta y = 55$ nm). Insets are the magnified images. (f–h) Cross-sectional counterparts of the SEM images in (c–e). The sizes of the NGMA/SGMAs are $a = 640$ nm, $h = 560/550$ nm, $t = 100$ nm, $w_1 = 270/255$ nm and $w_2 = 225$ nm, respectively. (c–h) Scale bars, 600 nm.

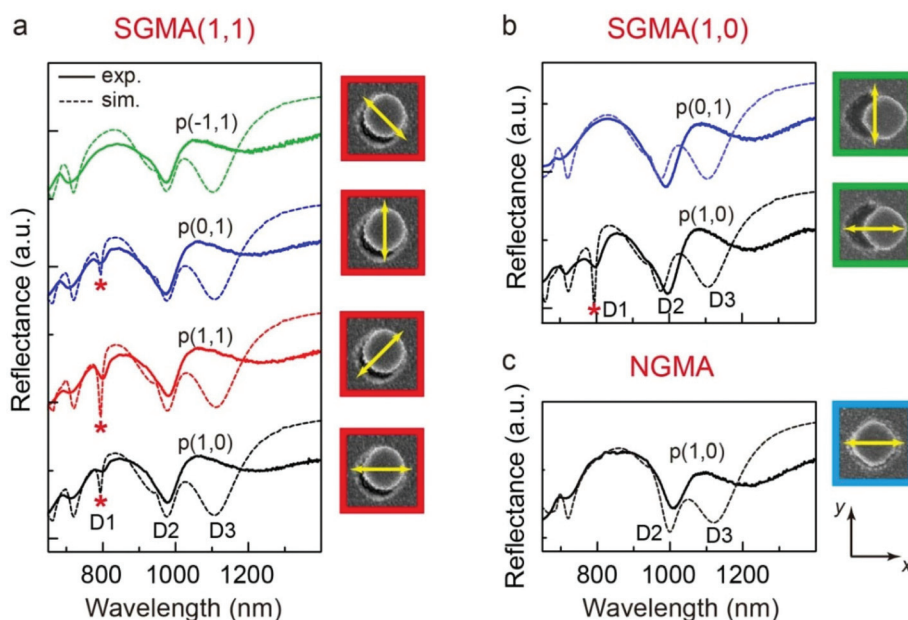


Fig. 3 Reflectance of the fabricated NGMA and SGMA under normal incidence. (a–c) Simulated (dashed curves) and experimental (solid curves) reflectance spectra for the SGMA(1,1) ($\Delta x = 55$ nm, $\Delta y = 55$ nm), SGMA(1,0) ($\Delta x = 100$ nm) and NGMA under normal incident light with various polarizations, respectively. Four polarizations, including p(1,0), p(1,1), p(0,1) and p(–1,1), are indicated by black, red, blue and green curves, respectively. The right images show the respective polarization orientations with respect to the directions of the dislocations in the NGMA/SGMA. The red asterisks in (a–c) indicate the unidirectional modes. The sizes of the NGMA/SGMA are $a = 640$ nm, $h = 560/550$ nm, $t = 100$ nm, $w_1 = 270/255$ nm and $w_2 = 225$ nm, respectively.

shown schematically in ESI Fig. S3.† In addition, a Glan-Taylor prism was employed in the optical path to generate linearly polarized incident waves with varying orientations. All reflectance spectra were corrected by dividing them with the reflectance spectrum of a silver mirror, which served strictly as a reference. As shown in Fig. 3c, two reflectance dips at the wavelengths of 972 and 1209 nm (marked by D2 and D3) are presented in the spectrum of NGMA, representing a Fabry-Pérot mode between the top/bottom gold layer and localized surface plasmon resonances (LSPRs) from the individual gold caps and holes (as revealed by the corresponding electric field intensity distributions in ESI Fig. S4†), respectively.⁴¹ In contrast to NGMA, an additional reflectance dip (marked by D1 and red asterisks) emerges in the SGMA(1,1) when illuminated by (1,0)-, (1,1)- and (0,1)-polarized waves (Fig. 3a) as well as the SGMA(1,0) under the illumination of the (1,0)-polarized wave (Fig. 3b), with a wavelength of around 800 nm, indicating the presence of a unidirectional mode. However, in the case that polarization of the incident wave is vertical to the orientation of the dislocation (*i.e.* SGMA(1,1) under (–1,1)-polarized illumination in Fig. 3a and SGMA(1,0) under (0,1)-polarized illumination in Fig. 3b), dip D1 doesn't exist, demonstrating the absence of a unidirectional mode. The experimental results are in agreement with FDTD simulations (dashed curves), confirming that the SGMA couple the incident light from free space into the unidirectional guided plasmon modes between top and bottom gold arrays as predicted. Note that the measured D3 has a longer wavelength than the simulated one.

This is due to the incongruity of the diagonals of the bottom gold holes in fabricated SGMA (the simulated reflection spectra of the SGMA(1,0) with varying diagonal lengths of caps/holes perpendicular to the polarization of the incident light and a fixed diagonal length of 360 nm parallel to the polarization as shown in ESI Fig. S5†). In addition, a relatively small dip D1 is present in the experiment, but not in the simulations. This deviation probably originates from imperfections in both the fabrication and reflectance measurement of the SGMA. For example, the surface scattering and grain boundary effects of the gold surface, shape inhomogeneity of mushrooms, and the beam divergence of $\sim 3^\circ$ on our UV/Vis/NIR spectrometer can all degrade the coupling strength of the waveguide mode, leading to a more shallow reflection dip.

To experimentally demonstrate the applications of SGMA as a switchable bi/tridirectional splitter, we collected the far-field images of the scattered light from the infinite mushroom arrays for a set of incident polarizations. Fig. 4a schematically shows the experimental set-up. A tunable mode locked Ti:sapphire femtosecond laser (Mai Tai, Spectra Physics, 690–1040 nm) was used to generate a pulse with a width of around 120 fs and a wavelength bandwidth of about 10 nm. A rotatable half-wave plate was inserted into the optical path to control the polarized direction of the linearly incident light. The samples were illuminated by the focused laser beam at the operating wavelength of 780 nm (the measurements under off-resonance excitations were also performed, see ESI Fig. S6†) and monitored through a homemade confocal optical

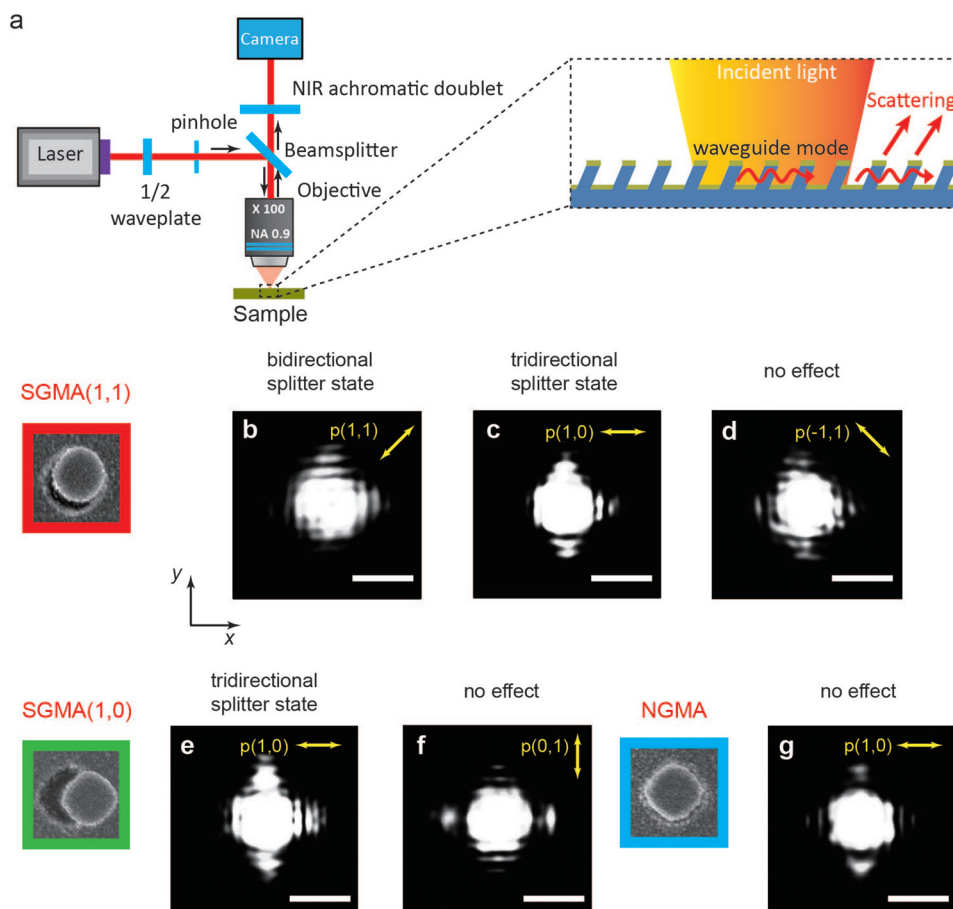


Fig. 4 Measurements of switchable SPP bi/tridirectional splitting based on the fabricated SGMA. (a) Schematic of set-up. A waveguide mode is directly launched via grating coupling with a focused Gaussian laser beam from free space with a wavelength of 780 nm. During the propagation, a fraction of the energy of the waveguide mode re-scatters back to the free space, and is finally captured by the camera. (b–d) Recorded images of SGMA(1,1) ($\Delta x = 55$ nm, $\Delta y = 55$ nm) under the normal incident light with the polarizations along (1,1), (1,0) and $(-1,1)$ directions, respectively. (e, f) Recorded images of SGMA(1,0) under the normal incident light with the polarizations along (1,0), and (0,1) directions, respectively. (g) Recorded image of NGMA under the normal incident light with the polarization along (1,0) direction. The sizes of the NGMA/SGMA are $a = 640$ nm, $h = 560/550$ nm, $t = 100$ nm, $w_1 = 270/255$ nm and $w_2 = 225$ nm, respectively. (b–g) Scale bars, 3000 nm.

microscope system with an objective lens ($\times 100$, $NA = 0.9$), where the far-field scattering images were captured by a camera (INFINITY 1-5, Lumenera Corporation). The diameter of the spot size on the samples is ~ 3000 nm. In this case, the collected light contains the direct back-scattering of the gold arrays as well as the leakage radiation of the coupled waveguide mode. Fig. 4b–d demonstrate that for a SGMA(1,1) ($\Delta x = 55$ nm, $\Delta y = 55$ nm), (1,1)-polarized incident light generates an orthogonally branched scattering pattern along the $+x$ and $+y$ directions ('bidirectional splitter' state, Fig. 4b), whereas (1,0)-polarized incident light launch the scattering along $+x$ and $\pm y$ directions ('tridirectional splitter' state, Fig. 4c). Interestingly, as the polarization is turned to $(-1,1)$, there is no observable directional splitting effect (Fig. 4d) as a result of the orthogonality between the incident electric field and the dislocation. These results match the corresponding simulated near-field distributions (Fig. 1g and h and ESI Fig. S7a†), further confirming the role of the polarization–dislocation interaction in our devices. Similar to the polarization-mediated beam-split-

ting of the SGMA(1,1), SGMA(1,0) ($\Delta x = 100$ nm, $\Delta y = 0$ nm) can also switch between producing unidirectional coupling or not by toggling between (1,0)- and (0,1)-polarized incident light (Fig. 4e and f), which is in an agreement with the simulated structures (Fig. 1i and ESI Fig. S7b†). For reference, no directionality is expected in NGMA ($\Delta x = 0$ nm, $\Delta y = 0$ nm) (ESI Fig. S7c†) and a symmetric scattering pattern takes place (Fig. 4g). Note that due to fabrication limitations, the SGMA in experiment were infinite structures instead of the finite structures containing only a few periods surrounded by a gold film in simulation, and a focused Gaussian beam rather than a collimated Gaussian beam was used (ESI Fig. S8†). Thus, the recorded images from the measured SGMA are not directly equivalent to the simulated electric field distributions. However, the experimental asymmetrical fringe patterns, appearing outside the laser spot region in Fig. 4, stem from the leakage radiation of the unidirectional waveguide mode, namely the light scattered into free space from the waveguide mode. In this regard, the recorded scattering signals corres-

pond to the SPP field in simulations and can be used to demonstrate the dependence of the SPP directionality upon the polarization of the incident light.

The unidirectional propagation of the SPPs observed in the SGMA can be explained by the interference between the scattered light from the gold cap array and the perforated gold film at the bottom of the structure due to the relative dislocation of these two arrays. The profile of the scattered light from the gold cap array for a particular guided mode can be expressed as

$$\psi_{\text{caps}}(\mathbf{s}) = Ae^{i\boldsymbol{\beta}\cdot\mathbf{s}} + Ae^{-i\boldsymbol{\beta}\cdot\mathbf{s}} \quad (2)$$

where A is the complex amplitude and $\boldsymbol{\beta} = \frac{2\pi}{a}(m_x, m_y)$ is the guide wave vector. These two terms represent waves moving in the $\pm\boldsymbol{\beta}$ direction with the same amplitude due to the symmetry of the gold cap layer. Likewise, the profile of the scattered light from the perforated gold film for the same guided mode is given by

$$\psi_{\text{film}}(\mathbf{s}) = Be^{i\boldsymbol{\beta}\cdot(\mathbf{s}+\Delta\mathbf{s})} + Be^{-i\boldsymbol{\beta}\cdot(\mathbf{s}+\Delta\mathbf{s})} \quad (3)$$

in which B is the complex amplitude and $\Delta\mathbf{s} = (\Delta x, \Delta y)$. Thus, despite the symmetry of each of the individual scattered portions, the total scattered field for the in-plane guided mode profile acquires direction-dependent amplitudes due to the interference of these two fields,

$$\psi_{\text{total}}(\mathbf{s}) = (A + Be^{i\boldsymbol{\beta}\cdot\Delta\mathbf{s}})e^{i\boldsymbol{\beta}\cdot\mathbf{s}} + (A + Be^{-i\boldsymbol{\beta}\cdot\Delta\mathbf{s}})e^{-i\boldsymbol{\beta}\cdot\mathbf{s}} \quad (4)$$

Therefore, many choices of $\boldsymbol{\beta}\cdot\Delta\mathbf{s}$ result in a net power flow in the $\pm\boldsymbol{\beta}$ direction, and the dislocation of the gold caps relative to the perforations in the gold film is shown to play a critical role in the unidirectional propagation of the SPPs generated by the SGMA. However, as mentioned above, the presence of a guided mode which satisfies eqn (1) for the wavelength of the incident light upon a structure with a sufficient dislocation is not enough to guarantee a unidirectional SPP. The incident light must also have a component of its polarization parallel to $\boldsymbol{\beta}$ for such an SPP to be launched. This is why the SGMA(1,1) when illuminated with (1,1)-polarized light was able to launch unidirectional SPPs in both the x and y directions, as $\boldsymbol{\beta}\cdot\Delta\mathbf{s}$ for this structure resulted in a net power flow for both of the degenerate, orthogonal modes, but was only able to launch a unidirectional SPP in the $+x$ direction when illuminated with x -polarized light, as the polarization was perpendicular to the guided mode along the y -axis.

In addition, we also note that such a SGMA seems to possess a relatively low coupling efficiency compared to a closely related periodic structure, the one-dimensional dislocated double-layered metal grating (DDMG) reported recently.⁴⁰ In Fig. 5, a side-by-side comparison of the near-field properties is presented to understand the physics behind the distinction between the unidirectional coupling efficiencies of the 1D and 2D structures. Fig. 5a and b display the simulated normal component (z -axis) distributions of the SPP electric field when a single aperture or slit in a gold film is illuminated with x -polarized light. Radial and linear patterns are visible,

corresponding to the SPP waves generated by the single aperture and slit, respectively. Due to the different scattering properties of the single unit cell, for the SGMA(1,0), only a fraction of light scattered by the gold caps and holes along $\pm x$ and $\pm y$ directions can be coupled to the waveguide modes, and the rest will be absorbed or re-scattered by the other neighboring gold mushrooms. This process results in a strong local field residing at the rims of the gold caps/apertures and inside the dielectric pillars (Fig. 5c). In this case, the propagating in-plane wave could be treated as a high order waveguide mode, which has a low coupling efficiency and higher radiation leakage. In contrast, for a DDMG, Fig. 5e shows a linear pattern along the x -axis at the air region between the pair of gold layers without integrating the background of the localized modes, indicating that it generates a nearly pure waveguide mode along only $\pm x$ directions. This mode is analogous to the lowest order waveguide mode, which has a high coupling efficiency and low radiation leakage. As a result, it can be expected that the DDMG has a much higher coupling efficiency than the SGMA(1,0) in the $+x$ direction. Furthermore, if we consider a SGMA(1,0) with a shrunken lattice spacing in the y -axis (actually as 1D grating of gold mushroom chains), it can be found that such a SGMA(1,0) acts as a 1D grating. A strong far-field coupling of dipoles occurs in $\pm x$ directions, shown in Fig. 5d, whereas it is suppressed in $\pm y$ directions, because the E_y component of the electric field is dominated by the near-field coupling rather than the far-field coupling for this case. This quasi-1D SGMA(1,0) exhibits a relatively large coupling efficiency in the $+x$ direction compared to the SGMA(1,0) in a square lattice, indicating an evolution from the high order waveguide mode to the lowest order mode. Finally, we performed simulations on the near-field intensity distributions and corresponding coupling efficiencies of the SGMA(1,0), quasi-1D SGMA(1,0) and DDMG with finite periods at the wavelengths with the largest extinction ratios, shown in Fig. 5f–k respectively. For the 2D SGMA(1,0) and quasi-1D SGMA(1,0), the total conversions of incident light coupling to the SPPs in $\pm x$ and $\pm y$ directions are roughly the same (9.62% and 10.55%), but specifically, the former couples the incident light to SPPs in $+x$ (4.52%) and $+/-y$ directions (both 2.28%), while the latter routes SPP to only $+x$ direction (8.98%). In comparison with the two SGMA above, DDMG shows a much higher coupling efficiency in the $+x$ direction (18.30%), due to most of the light coupled to the lowest waveguide mode along $+x$ directions without strong energy localization or radiation coupling in the orthogonal $\pm y$ directions. Therefore, there is actually a trade-off between the high unidirectional coupling efficiency and the capability of splitting light in the periodic array system. Thus, despite the sacrifice of the coupling efficiency, the SGMA provides a new degree of freedom to manipulate the SPPs in the orthogonal directions through tailoring the polarization–dislocation interaction. Endowed by this feature, the SGMA is particularly attractive and potentially applicable to plasmonic integrated circuits as a multiplexer and a router.

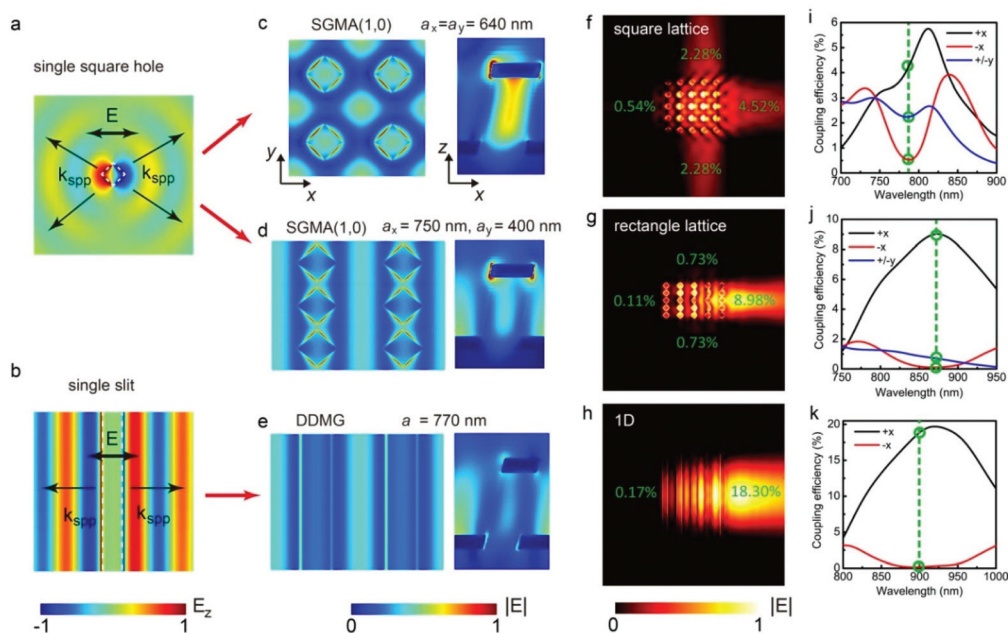


Fig. 5 Comparison of the near-field intensity distributions and unidirectional coupling efficiencies for the 1D and 2D dislocated double-layered gold gratings/arrays. (a, b) Simulated electric field E_z distributions of the single aperture or slit in a gold film launched by a plane-wave incident light polarized along the x -axis (indicated by black arrows) at the wavelengths of their scattering peaks. (c–e) Simulated electric field intensity distributions of the SGMA(1,0) in a square lattice, quasi-1D SGMA(1,0) and 1D DDMG at the wavelengths of the waveguide modes, respectively. The left and right columns correspond to an x - y plane 4 nm above the top surface of the bottom gold film and an x - z plane formed by cutting along the diagonal of the bottom square hole, respectively. (f–k) Simulated electric field intensity distributions and corresponding coupling efficiencies of the SGMA(1,0) in a square lattice, quasi-1D SGMA(1,0) and 1D DDMG with finite periods at the wavelengths with the optimal extinction ratios (indicated by the green dashed lines), respectively. The sizes of the single square aperture are $w_1 = 255$ nm, $t = 100$ nm, respectively. The sizes of the single slit are $w_1 = 270$ nm, $t = 100$ nm, respectively. The sizes of the SGMA(1,0) in a square lattice are $a_x = a_y = 640$ nm, $h = 550$ nm, $t = 100$ nm, $w_1 = 255$ nm, $w_2 = 225$ nm and $x = 100$ nm, respectively. The quasi-1D SGMA(1,0) has the same sizes except $a_x = 750$ nm and $a_y = 400$ nm. The sizes of the 1D DDMG are $a = 770$ nm, $h = 530$ nm, $t = 100$ nm, $w_1 = 270$ nm, $w_2 = 230$ nm and $\Delta x = 140$ nm, respectively.

Conclusions

In summary, we propose and demonstrate a multifunctional slanted gold mushroom array (1,1) as a bi/tridirectional splitter for SPP. The size of such a device is close to $3 \times 3 \mu\text{m}^2$, which is comparable to previous devices having only one of these functionalities.⁴² Furthermore, the SGMA(1,1) holds the promise of switchable SPP beam splitting/unidirectional coupling if one can manipulate the polarization of input waves. The mechanism of unidirectional coupling and polarization-controlled beam splitting for the SGMA arises from the in-plane dislocation between the upper layer gold cap array and the bottom layer gold hole array along the (1,1) direction. This dislocation leads to an additional phase difference for the incident light coupling to in-plane guided SPP modes *via* the gold cap array and gold hole array, resulting in constructive interference in one direction and destructive interference in the opposite direction, yielding a unidirectional coupler. By operating the SGMA(1,1) at its longest wavelength, which has degenerate propagating modes, incident light must result in unidirectional SPPs travelling in the (1,0), (0,1), or both directions. Thus, a polarization beam splitter is realized by tuning the polarization of the incident light, which will directly correspond to the magnitude of the SPP launched in each direction.

Acknowledgements

The authors acknowledge the financial support from the National Natural Science Foundation of China (11374376, 11174374, 11574406 and 11504437), the key project of DEGP (No. 2012CXZD0001), the U. S Air Force Office of Scientific Research (Grant No. FA9550-12-1-0024) and China Postdoctoral Science Foundation (2015M580745).

Notes and references

- 1 V. J. Sorger, R. F. Oulton, R.-M. Ma and X. Zhang, *MRS Bull.*, 2012, **37**, 728–738.
- 2 M. L. Brongersma and V. M. Shalaev, *Science*, 2010, **328**, 440–441.
- 3 E. Ozbay, *Science*, 2006, **311**, 189–193.
- 4 D. K. Gramotnev and S. I. Bozhevolnyi, *Nat. Photonics*, 2010, **4**, 83–91.
- 5 W. L. Barnes, A. Dereux and T. W. Ebbesen, *Nature*, 2003, **424**, 824–830.
- 6 F. J. Rodriguez-Fortuno, G. Marino, P. Ginzburg, D. O'connor, A. Martinez, G. A. Wurtz and A. V. Zayats, *Science*, 2013, **340**, 328–330.

- 7 J. Lin, J. P. Mueller, Q. Wang, G. Yuan, N. Antoniou, X. C. Yuan and F. Capasso, *Science*, 2013, **340**, 331–334.
- 8 L. Huang, X. Chen, B. Bai, Q. Tan, G. Jin, T. Zentgraf and S. Zhang, *Light: Sci. Appl.*, 2013, **2**, e70.
- 9 A. Pors, M. G. Nielsen, T. Bernardin, J.-C. Weeber and S. I. Bozhevolnyi, *Light: Sci. Appl.*, 2014, **3**, e197.
- 10 S.-Y. Lee, H. Yun, Y. Lee and B. Lee, *Laser Photonics Rev.*, 2014, **8**, 777–784.
- 11 L. Wang, T. Li, L. Li, W. Xia, X. G. Xu and S. N. Zhu, *Opt. Express*, 2012, **20**, 8710–8717.
- 12 J. Chen, Z. Li, M. Lei, S. Yue, J. Xiao and Q. Gong, *Opt. Express*, 2011, **19**, 26463–26469.
- 13 G. Di Martino, Y. Sonnefraud, S. Kena-Cohen, M. Tame, S. K. Ozdemir, M. S. Kim and S. A. Maier, *Nano Lett.*, 2012, **12**, 2504–2508.
- 14 D. Li, D. H. Zhang, C. Yan, T. Li, Y. Wang, Z. Xu, J. Wang and F. Qin, *Opt. Express*, 2013, **21**, 5949–5956.
- 15 T. Xu, Y. Zhao, D. Gan, C. Wang, C. Du and X. Luo, *Appl. Phys. Lett.*, 2008, **92**, 101501.
- 16 X. Huang and M. L. Brongersma, *Nano Lett.*, 2013, **13**, 5420–5424.
- 17 A. Baron, E. Devaux, J. C. Rodier, J. P. Hugonin, E. Rousseau, C. Genet, T. W. Ebbesen and P. Lalanne, *Nano Lett.*, 2011, **11**, 4207–4212.
- 18 Y. Liu, S. Palomba, Y. Park, T. Zentgraf, X. Yin and X. Zhang, *Nano Lett.*, 2012, **12**, 4853–4858.
- 19 G. Lerosey, D. F. Pile, P. Matheu, G. Bartal and X. Zhang, *Nano Lett.*, 2009, **9**, 327–331.
- 20 A. B. Evlyukhin, S. I. Bozhevolnyi, A. L. Stepanov and J. R. Krenn, *Appl. Phys. B*, 2006, **84**, 29–34.
- 21 H. Ditlbacher, J. R. Krenn, G. Schider, A. Leitner and F. R. Aussenegg, *Appl. Phys. Lett.*, 2002, **81**, 1762.
- 22 A. L. Stepanov, J. R. Krenn, H. Ditlbacher, A. Hohenau, A. Drezet, B. Steinberger, A. Leitner and F. R. Aussenegg, *Opt. Lett.*, 2005, **30**, 1524–1526.
- 23 J. R. Krenn, H. Ditlbacher, G. Schider, A. Hohenau, A. Leitner and F. R. Aussenegg, *J. Microsc.*, 2003, **209**, 167–172.
- 24 Z. Y. Yang and Y. F. Lu, *Opt. Express*, 2007, **15**, 9510.
- 25 S. Kumar, N. I. Kristiansen, A. Huck and U. L. Andersen, *Nano Lett.*, 2014, **14**, 663–669.
- 26 Q. Hu, D. H. Xu, Y. Zhou, R. W. Peng, R. H. Fan, N. X. Fang, Q. J. Wang, X. R. Huang and M. Wang, *Sci. Rep.*, 2013, **3**, 3095.
- 27 S.-Y. Lee, J. Park, I. Woo, N. Park and B. Lee, *Appl. Phys. Lett.*, 2010, **97**, 133113.
- 28 Y. Hwang, J.-E. Kim and H. Y. Park, *Opt. Commun.*, 2011, **284**, 4778–4781.
- 29 A. Drezet, D. Koller, A. Hohenau, A. Leitner, F. R. Aussenegg and J. R. Krenn, *Nano Lett.*, 2007, **7**, 1697–1700.
- 30 J. C. Weeber, M. U. González, A. L. Baudrion and A. Dereux, *Appl. Phys. Lett.*, 2005, **87**, 221101.
- 31 M. S. Kumar, X. Piao, S. Koo, S. Yu and N. Park, *Opt. Express*, 2010, **18**, 8800–8805.
- 32 Y. Fang, Z. Li, Y. Huang, S. Zhang, P. Nordlander, N. J. Halas and H. Xu, *Nano Lett.*, 2010, **10**, 1950–1954.
- 33 H. Wei, D. Pan and H. Xu, *Nanoscale*, 2015, **7**, 19053–19059.
- 34 Y. Fang and M. Sun, *Light: Sci. Appl.*, 2015, **4**, e294.
- 35 F. López-Tejiera, S. G. Rodrigo, L. Martín-Moreno, F. J. García-Vidal, E. Devaux, T. W. Ebbesen, J. R. Krenn, I. P. Radko, S. I. Bozhevolnyi, M. U. González, J. C. Weeber and A. Dereux, *Nat. Phys.*, 2007, **3**, 324–328.
- 36 S. Y. Lee, I. M. Lee, J. Park, S. Oh, W. Lee, K. Y. Kim and B. Lee, *Phys. Rev. Lett.*, 2012, **108**, 213907.
- 37 X. Zhang, Z. Li, J. Chen, S. Yue and Q. Gong, *Opt. Express*, 2013, **21**, 14548–14554.
- 38 Q. Gan and F. J. Bartoli, *Opt. Lett.*, 2010, **35**, 4181–4183.
- 39 A. E. Miroshnichenko and Y. S. Kivshar, *Science*, 2013, **340**, 283–284.
- 40 T. Liu, Y. Shen, W. Shin, Q. Zhu, S. Fan and C. Jin, *Nano Lett.*, 2014, **14**, 3848–3854.
- 41 Y. Shen, J. Zhou, T. Liu, Y. Tao, R. Jiang, M. Liu, G. Xiao, J. Zhu, Z. K. Zhou, X. Wang, C. Jin and J. Wang, *Nat. Commun.*, 2013, **4**, 2381.
- 42 B. Shen, P. Wang, R. Polson and R. Menon, *Nat. Photonics*, 2015, **9**, 378–382.